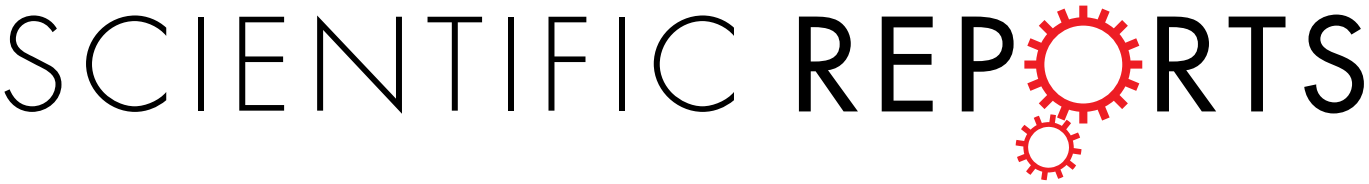

OPEN

Local Moment Instability of Os in Honeycomb $Li_{2.15}Os_{0.85}O_3$

M. K. Wallace[1], P. G. LaBarre[2], Jun Li[1], S.-T. Pi[3], W. E. Pickett[3], D. S. Dessau[4], D. Haskel[5], A. P. Ramirez[2] & M. A. Subramanian[1]

Received: 8 March 2018
Accepted: 13 April 2018
Published online: 26 April 2018

Compounds with honeycomb structures occupied by strong spin orbit coupled (SOC) moments are considered to be candidate Kitaev quantum spin liquids. Here we present the first example of Os on a honeycomb structure, $Li_{2.15(3)}Os_{0.85(3)}O_3$ ($C2/c$, $a = 5.09$ Å, $b = 8.81$ Å, $c = 9.83$ Å, $\beta = 99.3°$). Neutron diffraction shows large site disorder in the honeycomb layer and X-ray absorption spectroscopy indicates a valence state of Os (4.7 ± 0.2), consistent with the nominal concentration. We observe a transport band gap of $\Delta = 243 \pm 23$ meV, a large van Vleck susceptibility, and an effective moment of 0.85 μ_B, much lower than expected from 70% Os(+5). No evidence of long range order is found above 0.10 K but a spin glass-like peak in ac-susceptibility is observed at 0.5 K. The specific heat displays an impurity spin contribution in addition to a power law $\propto T^{(0.63 \pm 0.06)}$. Applied density functional theory (DFT) leads to a reduced moment, suggesting incipient itineracy of the valence electrons, and finding evidence that Li over stoichiometry leads to Os(4+)—Os(5+) mixed valence. This local picture is discussed in light of the site disorder and a possible underlying quantum spin liquid state.

The demonstration by Kitaev of an exactly solvable quantum spin liquid (QSL) model incorporating $S = \frac{1}{2}$ spins with anisotropic interactions on a honeycomb lattice[1,2] has motivated searches for its experimental realization. Whereas magnetic honeycomb-containing compounds have been extensively investigated in 3d and 4d metal oxides[3–11], the strong interaction anisotropy required by Kitaev's theory has placed a focus on 5d metal oxides, for which strong spin-orbit coupling (SOC), the origin of spatial anisotropy, can be expected[12–18]. In the A_2MO_3 honeycomb structure, where A is an alkali element and M a 4d or 5d element, the AM_2 layers form a hexagonal network of edge sharing MO_6 octahedra with a single A^+ ion at the centers of the hexagons (Fig. 1).

Examples such as α-Na_2IrO_3 and α-Li_2IrO_3 with effective spin $J_{eff} = \frac{1}{2}$, have recently emerged as possible examples of Kitaev physics. These compounds possess antiferromagnetic (AF) Weiss temperatures of 125(6) K and 33(3) K and undergo AF order at 15.5 K and 14.5 K for Na_2IrO_3 and Li_2IrO_3 respectively[19,20]. The 3D hyper-honeycomb lattice compound β-Li_2IrO_3, however, demonstrates a ferromagnetic (FM) Weiss temperature of 40 K and weak ordering signatures at 38 K among $J_{eff} = \frac{1}{2}$ moments[21]. Among non-oxide materials, the layered compound α -$RuCl_3$ has also been discussed as a possible Kitaev system, though it too undergoes long range order at 7.5 K[22]. Since the suppression of classical order via geometrical frustration is a requirement for creating a QSL state, the above systems, while possessing important attributes, fall short of the Kitaev criteria[23]. Due to the ordering seen in other honeycomb compounds and because the specific materials conditions required to produce a QSL are ill-defined at present, it is important to study other honeycomb-containing compounds with sizable SOC.

Here, we ask what would be the result of *reducing* the SOC from that of 540 meV in Ir to 480 meV in Os[24]. In the present work we report on the synthesis, structure, and properties of $Li_{2.15(3)}Os_{0.85(3)}O_3$ which is isostructural to the Ir honeycomb compounds mentioned above. For the stoichiometric compound, Li_2OsO_3, the Os ion is expected to be in the $4+ = d^4$, $J_{eff} = 0$ state to maintain charge-neutrality. In our work, we find, in contrast to other honeycomb systems, a lack of long range order above 0.1 K. While this might be due to a frustrated lattice, it also might be due to site disorder among the Os ions. For each crystallographic site representing the $LiOs_2$ layer, an average of 43% of the sites (compared to the expected 33 % of these sites) are occupied by lithium and thus the average valence of Os is $+4.5 \pm 0.1$ ($d^{3.5}$), a value consistent with our X-ray absorption spectroscopy (XAS) measurements, which yield $+4.7 \pm 0.2$. From a local moment perspective and using the XAS-determined valence state,

[1]Department of Chemistry, Oregon State University, Corvallis, OR, 97331, USA. [2]Department of Physics, University of California Santa Cruz, Santa Cruz, CA, 95064, USA. [3]Department of Physics, University of California Davis, Davis, CA, 95616, USA. [4]Department of Physics, University of Colorado, Denver, CO, 80309, USA. [5]Advanced Photon Source, Argonne National Laboratory, Argonne, IL, 60439, USA. Correspondence and requests for materials should be addressed to M.A.S. (email: mas.subramanian@oregonstate.edu)

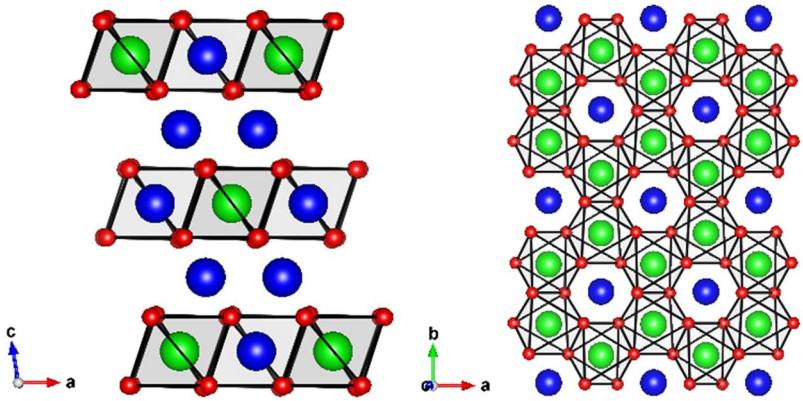

Figure 1. Left: Li_2MO_3 (M = 4d or 5d element) structure as alternating Li and LiM_2 layers. Right: Viewed along the c axis the LiM_2 layer, where MO_6 edge-sharing octahedra form the honeycomb lattice. Blue, green, and red spheres represent lithium, metal, and oxygen atoms respectively.

our system might be comprised of 30% d^4 ($J_{eff}=0$) and 70% d^5 ($J_{eff}=\frac{3}{2}$) but its physical properties are not easily understood. We find a transport gap of 243 meV, an effective magnetic moment of 0.85 μ_B, which is much less than the effective moment of 3.24 μ_B expected if 70 % of the ions possessed $J_{eff}=\frac{3}{2}$. No magnetic order is observed above 0.10 K, and the specific heat obeys a fractional power law in temperature and is only weakly magnetic field-dependent. We discuss the constraints on the local physics of Os from a band structure perspective and their implications for collective behavior en route to a possible QSL in SOC honeycomb systems.

Results and Discussion

Structure. Common space groups assigned to honeycomb-structure compounds Li_2MO_3 (M = Mo, Mn, Rh, Ir, Ru, Pt, and Sn) are *C*2/*m*, *C*2/*c*, and $R\bar{3}m$[4,7–9,11,17,25–32]. Supplemental Figure S1 represents Li_2MO_3 *C*2/*m*, *C*2/*c*, and $R\bar{3}m$ unit cells illustrated down the b-axis (top) and corresponding portion of the Li-M layer representing a (bottom) with lithium and metal occupying their ideal Wyckoff positions[4,11,17,28,29,32]. For all three space groups, edge sharing octahedral LiM_2 layers alternate with edge sharing octahedral Li layers. The difference in space groups and their associated symmetries can in part be ascribed to stacking of the LiM_2 layers, with $R\bar{3}m$ as the highest in symmetry. The space group assignments of some Li_2MO_3 systems has been controversial. For example, Li_2MnO_3 was first refined to be *C*2/*c*, but later found to be *C*2/*m* on the basis of electron diffraction and transmission electron microscopy[26,27].

Another example is Li_2MoO_3, which was reported as both *C*2/*c* and $R\bar{3}m$[4,28]. When comparing literature on polycrystalline Li_2IrO_3 synthesized under standard solid state conditions, discrepancies in *C*2/*c* and *C*2/*m* space groups exist. Recent work supports the higher symmetry *C*2/*m* as the appropriate space group for polycrystalline Li_2IrO_3[17,29,32]. The powder X-ray diffraction pattern of Li_2OsO_3 is shown in Fig. 2 (top black line).

At first glance, the X-ray pattern pointed to a more symmetric space group, $R\bar{3}m$, however, close examination of the pattern showed weak and broad diffraction peaks in the 2θ region of 19° to 33°. It is known that for both *C*2/*m* and *C*2/*c* systems, with no Li-M site exchange within the LiM_2 layers, sharp peaks exist within the 19° to 33° range. However, introducing Li-M site exchange within the LiM_2 layers decreases the relative intensities of these peaks, leading to virtually no peak presence at 30% Li-M site exchange[30]. Such a reduction in diffraction peak intensity is also found for (hk0) reflections past 38°[30]. Disorder among Li-M sites is commonly reported for honeycomb layered metal oxides since all corresponding crystallographic sites are octahedral and similar in size[4,9,11,17,18,26–28]. The presence of stacking faults associated with a shift between successive LiM_2 layers will cause the peaks in the region from 19° to 33° to further broaden asymmetrically[7–9,18,30]. Thus, with the existence of Li-M site disorder and stacking faults, it is difficult to distinguish between the corresponding space groups using powder X-ray diffraction. The x-ray scattering length for lithium and oxygen are also small due to their low *Z*. Because of the neutron scattering lengths of lithium, osmium, and oxygen, neutron diffraction is ideal to characterize the Li_2OsO_3 structure.

To determine the crystal structure, Rietveld refinements were performed on room temperature neutron diffraction data using the GSAS program (Fig. 3)[33,34]. The current synthesis procedure restricted diffraction measurements to the Oak Ridge NOMAD TOF Neutron beamline, which is well-suited for small sample sizes. A pseudo-Voigt peak shape profile was chosen and parameters refined to obtain the best fit to the collected data. The space group was refined to be *C*2/*c*, with lattice dimensions $a=5.09$ Å, $b=8.81$ Å, $c=9.83$ Å, and $\beta=99.3°$. Rietveld refinements for all collected banks are shown in Supplemental Figure S2, with cumulative $wR_p=6.40$ %. The atomic coordinates, occupancies, and isotropic displacement parameters are represented in Table 1.

Interatomic distances and angles are given in Supplemental Table S1. No osmium is detected in the lithium-only layers. For *C*2/*c* there are three unique atomic positions to describe the Li and Os sites within the $LiOs_2$ layer (Supplemental Figure S3). Shown in Table 1, corresponding sites are labeled as Li/Os 3, 4, and 5. If no Li-Os site disorder existed within the $LiOs_2$ layer, only Li3, Os4, and Os5 would exist (each with an occupancy of

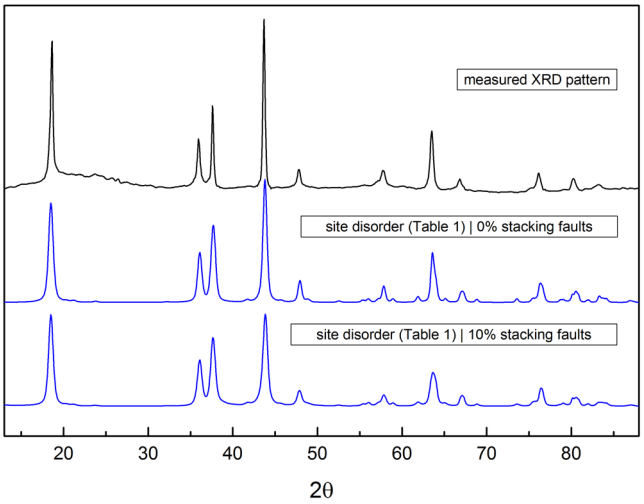

Figure 2. A comparison of the measured XRD pattern (top black line) ($\lambda = 1.514$ Angstroms), along with 43% site disorder (Table 1) |0% stacking fault and 43% site disorder (Table 1) |10% stacking fault simulated DIFFaX patterns (blue lines).

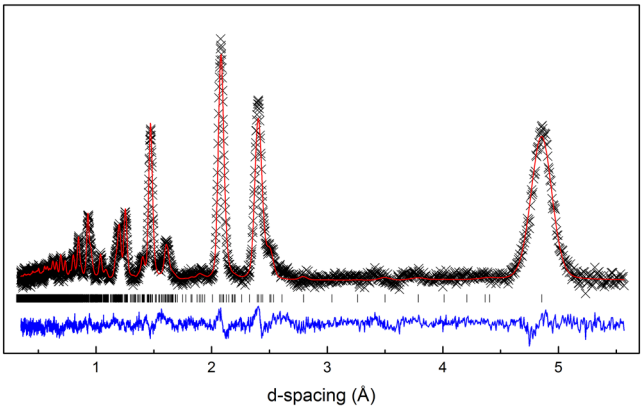

Figure 3. Rietveld refinement of TOF Neutron (Oak Ridge NOMAD BL-1B) diffraction data. The collected data (black cross), Rietveld refinement (red line), and difference (blue line) are presented for one of the four collected banks. Resulting cumulative $wR_p = 6.4\,\%$.

	Wyckoff	*x*	*y*	*z*	*occ*	U_{iso}
Li1	8*f*	0.2543(2)	0.0840(1)	0.0044(9)	1	0.25(8)
Li2	4*d*	0.25	0.25	0.5	1	0.037(4)
Li3	4*e*	0	0.7531(8)	0.25	0.32(4)	0.20(7)
Os3	4*e*	0	0.7531(8)	0.25	0.68(4)	0.20(7)
Os4	4*e*	0	0.0777(7)	0.25	0.46(2)	0.0043(2)
Li4	4*e*	0	0.0777(7)	0.25	0.54(2)	0.0043(2)
Os5	4*e*	0	0.4026(6)	0.25	0.56(2)	0.0082(2)
Li5	4*e*	0	0.4026(6)	0.25	0.44(2)	0.0082(2)
O1	8*f*	0.1335(7)	0.2414(5)	0.1344(4)	1	0.029(3)
O2	8*f*	0.1269(8)	0.5770(5)	0.1414(4)	1	0.0085(3)
O3	8*f*	0.1387(8)	0.9181(5)	0.1332(5)	1	0.0082(8)

Table 1. Atomic coordinates, occupancies and isotropic displacement parameters obtained from Rietveld refinement (*C*2/*c*) of TOF Neutron (Oak Ridge NOMAD BL-1B) diffraction data.

1), with Os4 and Os5 sites describing the honeycomb rings. As shown from Table 1 occupancies, a large percentage of Li-Os site disorder exists within the $LiOs_2$ layer. For each of the three respective crystallographic sites, an average of 43% is occupied by lithium. The stoichiometry derived from occupancy refinements of Li, Os, and O is

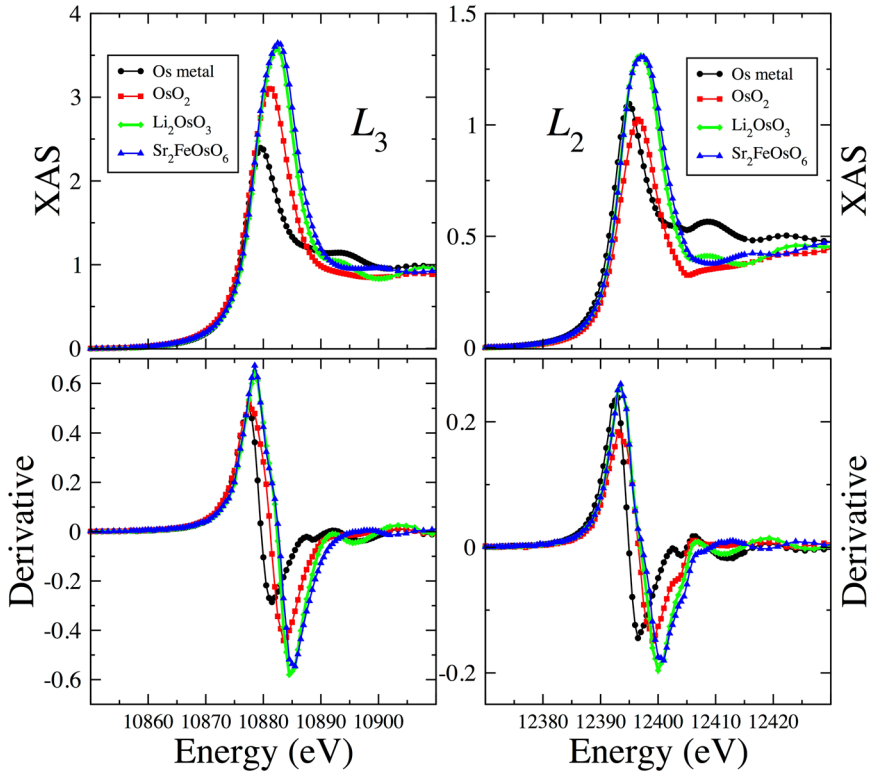

Figure 4. XAS measurements at the Os $L_{2,3}$ absorption edges on $Li_{2.15}Os_{0.85}O_3$ and three reference compounds with known oxidation state.

$Li_{2\cdot15(3)}Os_{0.85(3)}O_3$ suggesting an average osmium oxidation state of 4.5 ± 0.1. It is important to note that oxygen occupancy refinements indicate that the oxygen sites are fully occupied and no detectable vacancies are observed. Though 2:1 stoichiometric amounts of Li:Os were used in the synthesis, the refined stoichiometric ratio is considered reasonable as the presence of a small amount of osmium impurity is formed during the synthesis and was removed by heating the sample in air at 300 °C as OsO_4 through sublimation.

Stacking faults were modeled using the DIFFaX program[35] and the description of the model and analogous XRD patterns are discussed in the SI section. From the discussion presented, the absence of the (020) peak can only be attributed to Li-Os site disorder within the $LiOs_2$ layers and not from stacking faults, consistent with the neutron refinement. As shown in Fig. 2, the measured XRD pattern is compared to simulated DIFFaX patterns with site disorder representing Table 1 refined Wyckoff site occupancies with and without 10% stacking faults (blue lines).

XAS measurements at the Os $L_{2,3}$ absorption edges ($2p_{\frac{1}{2},\frac{3}{2}} \rightarrow 5d$ resonant excitation) were used to provide an additional estimate of Os valence (Fig. 4). The enhanced X-ray absorption above the leading edge ("white line") is a result of large density of empty 5d states near the Fermi level. This peak grows in intensity and shifts to higher energy with increasing Os oxidation state. Interpolating the XAS peak position in the honeycomb sample onto those of the reference compounds yields an oxidation state of $+4.7 \pm 0.2$, within errors of results from structure refinements.

The ratio of L_3 to L_2 white line intensity, also known as the isotropic branching ratio (BR), provides a measure of the relevance of SOC interactions in the 5d band[36,37]. In the absence of sizable SOC interactions, the isotropic branching ratio equals 2 reflecting the different occupancies of the core levels at L_3 and L_2 edges. We measured $BR = 2.9(1)$ which significantly differs from the statistical value of 2 and indicates that SOC interactions need to be included in order to describe the 5d electronic structure of this compound.

Thermodynamic and Transport Properties. Temperature dependent resistivity and Seebeck measurements from 300–600 Kelvin are shown in Fig. 5. The gap energy (E_g) for the sample was extracted using $\rho = \rho_o \exp(E_g/2k_BT)$ with $E_g = 220$ meV and 266 meV obtained from low- and high-temperature transport measurements respectively, thus indicating a small band gap insulator (Fig. 5 - right).

The magnetic susceptibility, χ_{dc}, for $H = 0.5$ T (Fig. 6) suggests the combined effects of Curie-Weiss as well as van Vleck temperature independent paramagnetism over the entire measurement range above 2 K. Within this assumption, we varied the magnitude of the van Vleck term, χ_{VV}, to produce a pure Curie-Weiss contribution. We found that subtractin $\chi_{VV} = 0.00135$ emu/mole from the measured $\chi(T)$ produces the straightest $1/\chi(T)$, resulting in a good fit to the Curie-Weiss form, $\chi = C/(T - \theta)$, where C is the Curie constant and, θ is the Weiss constant.

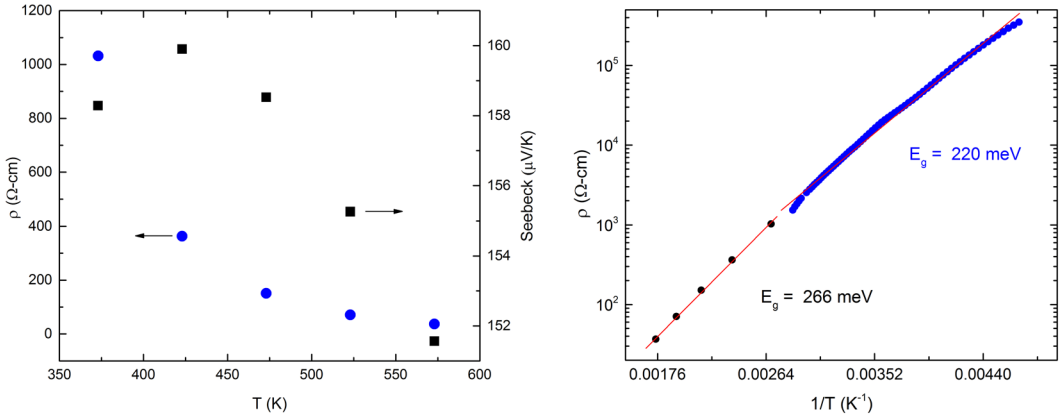

Figure 5. Left: High temperature resistivity and Seebeck coefficient data of $Li_{2.15}Os_{0.85}O_3$ sample from 350 to 600 K. Right: Resistivity versus temperature for $Li_{2.15}Os_{0.85}O_3$ in the range 200–600 K versus inverse temperature. The low and high temperature measurements were performed in different apparatuses on samples from the same growth run. To assure continuity at T = 300 K, the data have been rescaled for the low temperature measurement due to its greater uncertainty in the geometric factor.

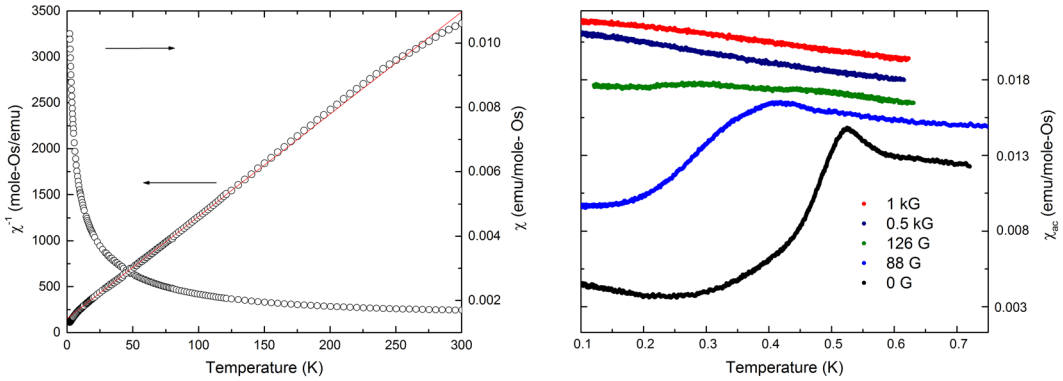

Figure 6. Left: DC-Susceptibility $Li_{2.15}Os_{0.85}O_3$ versus temperature. Also shown is the inverse susceptibility after subtracting a van Vleck term as described in the text. Right: ac-susceptibility versus temperature at different values of applied magnetic field. The curves have been offset vertically by 0.0020, 0.0032, 0.0044, and 0.0056 emu for $H = 88$, 126, 500, and 1000 G respectively, for clarity.

Fitting the data between 50 and 200 K yields a Weiss constant of $\theta = -11.5$ K and a finite effective moment $\mu_{eff} = 0.85\ \mu_B$, significantly greater than expected for the $J_{eff} = 0$ state of Os(+4). Given the above XAS and neutron scattering refinement results showing that the average Os valence is 4.7, however, an alternate ionic scenario is for 70% of the Os ions to be in the +5 state ($J_{eff} = \frac{3}{2}$) and 30% in the +4 state ($J_{eff} = 0$). This analysis yields $\mu_{\text{eff}} = 1.01\ \mu_B$ ($\theta = -11.8$ K) for the magnetic (+5) ions, which is now significantly less than the expected moment.

We discuss possible sources of this discrepancy below. These χ_{dc} data were augmented with ac-susceptibility (χ_{ac}) data down to 0.1 K, which were calibrated to the χ_{dc} data in the overlapping temperature range 2.0–2.5 K. A peak in χ_{ac} is observed at 0.5 K, but is rapidly suppressed by magnetic fields far less than 0.1 T. Given the usual relationship between H and T for a g-factor of two, one expects suppression of an antiferromagnetic ordering feature at 0.5 K for H values an order of magnitude larger than observed. Alternatively, such a cusp in χ_{ac} can be attributed to spin glass freezing, a scenario consistent with the high degree of disorder in this spin system. The spins involved in such freezing may not represent the bulk of the Os(+5) spin population, as we argue below.

The existence of a small subset of spins that are interacting at a mean field energy scale of k_BT for T = 0.5 K, as suggested by the χ_{ac} peak, is also supported by $C(T, H)$, shown in Fig. 7. Here, C/T exhibits an upturn below its minimum at T = 6 K. This upturn is only moderately affected by fields up to 8 T, so we model this as $C = C_1(T) + C_2(T, H)$. Here C_1 is a combination of the lattice specific heat and an H-independent electronic contribution. Taking the difference between $C(H = 8\text{ T})$ and $C(H = 0)$, we find that $C_2(T, H = 8\text{ T})$ resembles a broadened Schottky anomaly (Fig. 7 upper inset). We can fit this contribution to either a single $J_{eff} = \frac{3}{2}$ (g = 1.3) Schottky anomaly or a pair of $J_{eff} = \frac{1}{2}$ (g = 2.6 and 7.4) Schottky anomalies with molar concentrations of 4.1% and 9.6% (total for the pair) respectively (Assuming 70 % of the spins are magnetic, these fractions become 5.9% and 13.7%). Thus, it is not unlikely that the spins undergoing spin-glass-like freezing are the same spins responsible for the Curie-tail susceptibility. We now turn to the $C1(T)$ term, which is calculated using the two different

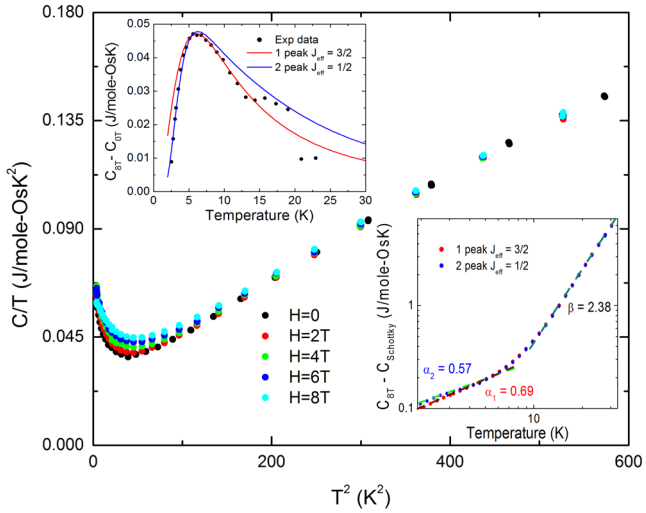

Figure 7. The specific heat C(T) of $Li_{2.15}Os_{0.85}O_3$ in various applied fields, measured using a Physical Property Measurement System. Upper Inset: Impurity spins modeled with a Schottky anomaly. Lower Inset: Specific heat after removing the impurity contribution.

Schottky approximations mentioned above and plotted in the lower inset of Fig. 7. We note that, below 8 K, $C_l(T) \propto T^{\alpha}$, where $\alpha = 0.69$ and 0.57 for the $J_{eff} = \frac{3}{2}$ and $\frac{1}{2}$ Schottky analyses respectively. Such a sublinear form cannot persist down to the lowest temperatures, and importantly is clearly distinct from the phonon contribution visible above 8 K. At the same time, it appears that, among the 70% of Os ions that are in a +5 state (within an ionic picture) and thus possibly magnetic, less than 15% are accounted for in either susceptibility or field-dependent specific heat. If the sublinear low-T contribution is due to these unaccounted for, but nevertheless magnetic, Os(+5) ions, then they must be in a type of singlet state due to exchange interactions with a strength greater than the Zeeman energy of an 8 Tesla field, but of a type that invalidates the effective moment approximation below room temperature.

Electronic structure. Early model treatments of 5d oxides on honeycomb lattices built on the ionic description of crystal field splitting, additionally with strong SOC among orbitals, focused attention on the t_{2g} subshell $J_{eff} = \frac{1}{2}$ and $\frac{3}{2}$ subspaces. The relevant energy scales of individual bandwidth W, Hubbard U, Hund's JH, and SOC strength ξ, all lie in the 0.5–1.5 eV range, and studies of the electronic structure and especially the exchange coupling have concluded that the ionic picture provides a challenging starting point at best. The electronic structure of octahedral osmates is complicated by several features. First, the active t_{2g} orbitals are strongly hybridized with the oxygen 2p orbitals, resulting in strongly coupled Os 5d − O 2p states as the fundamental chemical unit. Osmates in the Ba_2NaOsO_6 family, for example, have half of the spin density residing on the O octahedron[38,39]. Iridates behave similarly, leading to their characterization as *molecular orbital compounds*, which can lead to longer range exchange coupling parameters compared to more localized moments[40]. Second, SOC also affects the electronic structure, creating both single-ion as well as exchange anisotropy, the relative effects of which are difficult to disentangle. Third, the distortion from ideal rhombohedral symmetry introduces new lower symmetry Fourier components of the potential that causes band anti-crossings. These in turn result in very narrow, 0.3 eV, individual bandwidths and the likelihood of small gaps, as shown below.

Several theoretical studies of honeycomb iridates have concluded that magnetic interactions beyond the Heisenberg-Kitaev model are important, suggesting a more itinerant picture of the electronic structure[19,41–46]. Many of the general findings for iridates carry over to osmates. Our compound presents the additional complication of Os possessing a nominal valence of +4.7, so one must consider a mixture of d^3 with d^4 ions. The ionic picture of d^4 begins with a non-magnetic $J_{eff} = 0$ ion and for d^3 the ionic value is $J_{eff} = \frac{3}{2}$, and the insulating nature suggests these different ionic states reside on distinct lattice sites, as opposed to the intermediate valence picture. In this ionic picture, the measured $\mu_{eff} = 0.85\ \mu_B$ is challenging to account for, as mentioned above, which leads us to consider the general question of moment formation in nearly itinerant systems.

In an effort to reconcile the valence state measurements with the magneto-thermal measurements, we have applied density functional theory (DFT) methods including SOC, correlation effects, and a fixed atomic spin moment method in our study of Li_2OsO_3 (see Methods for the description)[47–52]. Without magnetism, SOC is strong enough to provide a pseudogap but no gap, within the Os t_{2g} bands. This SOC-driven separation is compromised by crystal subfield splittings, bandwidth effects, and anti-crossings arising from structural distortion away from rhombohedral symmetry leaving two inequivalent Os sites. The resulting band structure (not shown) is that of a very narrow, essentially zero (indirect) gap semiconductor. Due to the molecular orbital nature of the t_{2g} band complex, intra-atomic repulsion effects as treated by the Hubbard U repulsion are ineffective in opening a gap, for reasonable values of U (2 eV or less). Antiferromagnetic order tends to encourage gap opening, producing Os moments of 0.3 μ_B.

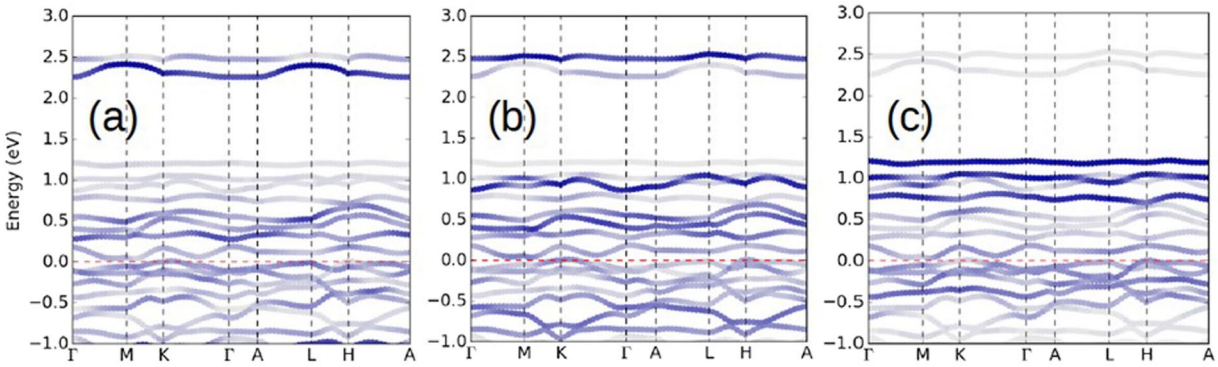

Figure 8. Plot of bands in the Os t_{2g} region of 25% Li-substituted Li_2OsO_3 on the Os honeycomb sublattice, with energy zero (horizontal red dashed line) denoting the gap region. The fatbands plots emphasize the Os 5d character on (**a**) the Os[0] site with no Li neighbor, (**b**) the Os[1] site with one Li neighbor, and (**c**) the Os[2] site with two Li neighbors. While Os[0] and Os[1] show some differences, Os[2] is qualitatively different.

To include in the modeling the effect of the observed Os moment, we have adopted the constrained atomic moment method as implemented in the *abinit* code[47]. This method proceeds not by specifying a value for U for the Os 5d orbitals, but by fixing the spin moment by applying an intra-atomic Zeeman field determined self-consistently; both magnitude and direction can be specified separately for any atom. Magnitudes of 0.8 μ_B and 0.5 μ_B have been studied; the latter value represents the ordered component expected of a 0.8 μ_B local (C-W) moment. Bandgaps of 0.25 eV and larger were obtained, depending weakly on the imposed moment but strongly on the magnetic alignment (the larger ones were for AFM order). The resulting orbital moments are minor, only a few hundredths of 1 μ_B, independent of the chosen direction of spin. These results do not fit that of a Mott insulator: there is no robust local moment, and Hubbard U is not needed to open a gap and has little effect on the size of the gap. Thus our model rationalizes the observations of a narrow transport gap and small magnetic moment in $Li_{2.15}Os_{0.85}O_3$.

Due to intermixing of Li on the Os honeycomb lattice, we have made an initial study of the effect of intermixing, by replacing 25% of the Os sublattice by Li while keeping the Li sublattice intact. The Os moments are fixed with magnitude 0.8 μ_B and oriented along separate (111) axes to mimic disordered moments. The resulting band structure, shown in Fig. 8, illustrates the flat individual bands that arise, and that a very small gap exists or is imminent, depending on details of the calculations. The bands are not significantly different in appearance from those of Li_2OsO_3.

We now focus on the effect of Li substitution on the remaining Os ions. This 25% replacement results in three Os sites, denoted by Os[j] which has j Li neighbors, j = 0, 1 or 2. The formal valences of Os in this $Li_2(Li_{1/4}Os_{3/4})O_3$ structure should average to 5+. The periodicity leaves Os[0]-Os[1] chains and comparatively isolated Os[2] ions, which in addition to two Li neighbors the Os neighbor is at a long Os-Os separation. The spectral distribution of Os[2] in Fig. 8 is substantially different from the other two, more representative of a lower oxidation state. While simple electron count indicates that Li substitution must oxidize some Os ions, having two Li neighbors strongly affects the formal valence of the Os ion.

This modeling illustrates that the Os valence is sensitive not only to the total charge available, but also to the local environment. Different valence states carry different moments, and sensitivity to the local environment suggests that variation of exchange constants promotes a frustration of magnetic order. Note in Fig. 8 that the spectral distributions of 5d weight are significantly different for Os[0] and Os[1], while that of Os[2] is less weight in the occupied bands. This implication then is that of one Os(4+) ions and two Os(5+) ion, with an average valence of 4.67 consistent with spectroscopic evidence on our samples. More of a specific nature cannot be concluded because the Os moments were constrained (to be equal), whereas those of different valence states would not be equal.

Summary

We have presented the first example of Os on a honeycomb structure, $Li_{2.15(3)}Os_{0.85(3)}O_3$, and have characterized it with atomic, structural, and magneto-thermal probes. The Os ions have an average valence state of +4.7 and large site disorder exists in the honeycomb layers. This compound is a narrow band gap semiconductor. The magnetic susceptibility and specific heat present a picture in which the effective Os moment is reduced to a value well below that expected from the valence-state measurements, which suggests that the valence electrons are on the verge of itineracy, a conclusion supported by our density functional theory calculations. These results strongly suggest that spin orbit coupling of Os is playing an important role in the collective electronic behavior of this honeycomb system, and that further studies of osmates on frustrating lattices are warranted.

Methods

Synthesis and Structure Characterization. Stoichiometric amounts of Li_2CO_3 and OsO_2 (synthesized from osmium metal) were intimately ground, pressed into a pellet, loaded into an alumina crucible, and fired in a tube furnace at 700 C under Argon flow. Firing was repeated to 850 C with 50 C increments, grinding the sample

before each firing. Each firing was performed under argon flow. Phase analysis of the powder samples was performed by X-ray diffraction using a Rigaku MiniFlex II diffractometer with Cu Kα radiation and a graphite monochromator for the diffracted beam. Time of Flight (TOF) neutron diffraction measurements were collected at ORNL NOMAD BL-1B SNS beamline. X-ray absorption spectroscopy measurements were carried out at beamline 4-ID-D of the Advanced Photon Source at Argonne National Laboratory using a transmission geometry. Reference samples for valence determination included Os metal, $Os^{4+}O_2$ and $Sr_2FeOs^{5+}O_6$[53].

Electronic and Thermal Properties. The Seebeck coefficient and electrical conductivity data (350 K–600 K) were collected on an ULVAC ZEM-3 under a helium atmosphere. Magnetization measurements (2 K–300 K) were obtained with a Quantum Design MPMS. Resistivity, $\rho(T)$, (200 K–350 K) and specific heat, $C(T)$, data (2 K–30 K) were obtained using a Quantum Design PPMS. Magnetic ac-susceptibility data down to 0.1 K were obtained in a ^{3}He-^{4}He dilution refrigerator with thermal contact to the mixing chamber made via a copper wire bundle bonded to the sample with Stycast 1266 epoxy. Data were obtained at 143 Hz and with an excitation current low enough to eliminate heating from the coils.

Theoretical Methods. We use the open-source package ABINIT[48] to perform electronic calculations, with the generalized gradient approximation (GGA)[49] for the semilocal exchange-correlation functional and the projector augmented wave method (PAW)[50] for core electrons. A Hubbard U repulsive interaction was applied with magnitude as indicated, Hund's JH = 0.4 eV was applied, on the Os 5d orbitals[51]. A mesh of $9 \times 5 \times 9$ was used for k-sampling and 500 eV for energy cutoff. The constrained atomic spin moment on Os method[52] was used in some calculations to fix moments at or near the observed value. Constraints are managed by the use of Lagrangian multipliers, imposed with constraint parameters; the input parameter $\lambda = 1.0$ was used[48].

References

1. Khaliullin, G. Excitonic magnetism in van vleck-type d^4 mott insulators. *Physical Review Letters* **111**, 197201 (2013).
2. Kitaev, A. Anyons in an exactly solved model and beyond. *Annals of Physics* **321**, 2–111 (2006).
3. Felner, I. & Bradarić, I. M. The magnetic behavior of Li_2MO_3 (M = Mn, Ru and Ir) and $Li_2(Mn_{1-x}Ru_x)O_3$. *Physica B: Condensed Matter* **311**, 195–199 (2002).
4. James, A. C. W. P. & Goodenough, J. Structure and bonding in Li_2MoO_3 and $Li_{2-x}MoO_3$ ($0 \leq x \leq 1.7$). *J. Solid State Chem.* **76**, 87–96 (1988).
5. Lee, S. *et al*. Antiferromagnetic ordering in Li_2MnO_3 single crystals with a two-dimensional honeycomb lattice. *Journal of Physics: Condensed Matter* **24**, 456004 (2012).
6. Wang, J. C. *et al*. Lattice-tuned magnetism of $Ru^4 + (4d^4)$ ions in single-crystals of the layered honeycomb ruthenates: Li_2RuO_3 and Na_2RuO_3. *Phys. Rev. B.* **90**, 161110 (2014).
7. Breger, J. *et al*. High-resolution X-ray diffraction, DIFFaX, NMR and first principles study of disorder in the Li_2MnO_3-$Li[Ni_{1/2}Mn_{1/2}]O_2$ solid solution. *J. Solid State Chem.* **178**, 2575–2585 (2005).
8. Schmidt, W., Berthelot, R., Etienne, L., Wattiaux, A. & Subramanian, M. A. Synthesis and characterization of O_3-$Na_3LiFeSbO_6$: A new honeycomb ordered layered oxide. *Mater. Res. Bull.* **50**, 292–296 (2014).
9. Lu, Z. & Dahn, J. R. Effects of stacking fault defects on the X-ray diffraction patterns of T_2, O_2, and O_6 structure $Li_{2/3}[CoxNi_{1/3-x}Mn_{2/3}]O_2$. *Chemistry of Materials* **13**, 2078–2083 (2001).
10. Torres-Castro, L., Abreu-Sepulveda, M. A., Katiyar, R. S. & Manivannan, A. Electrochemical investigations on the effect of Mg-substitution in Li_2MnO_3 cathode. *Journal of the Electrochemical Society* **164**, A1464–A1473 (2017).
11. Hodeau, J. L., Marezio, M., Santoro, A. & Roth, R. S. Neutron profile refinement of the structures of Li_2SnO_3 and Li_2ZrO_3. *Journal of Solid State Chemistry* **45**, 170–179 (1982).
12. Manni, S. *et al*. Effect of isoelectronic doping on honeycomb lattice iridate A_2IrO_3. *Phys. Rev. B.* **89**, 1–7 (2014).
13. Singh, Y. & Gegenwart, P. Antiferromagnetic mott insulating state in single crystals of the honeycomb lattice material. *Phys. Rev. B.* **82**, 1–7 (2010).
14. Mccalla, E. *et al*. Visualization of O-O peroxo-like dimers in high-capacity layered oxides for li-ion batteries. *Science* **350**, 1516–1521 (2015).
15. Okada, S. *et al*. Cathode characteristics of layered rocksalt oxide, Li_2PtO_3. *Electrochim. Acta.* **45**, 329–334 (1999).
16. Baklanova, Y. V. *et al*. Photo- and radioluminescence of lithium hafnate Li_2HfO_3. *Optical Materials* **34**, 1037–1041 (2012).
17. Kobayashi, H., Tabuchi, M., Shikano, M., Kageyama, H. & Kanno, R. Structure, and magnetic and electrochemical properties of layered oxides, Li_2IrO_3. *J. Mater. Chem.* **13**, 957–962 (2003).
18. Kumari, S. L. *et al*. Charge transfer instability in a mixed Ir/Rh honeycomb lattice in $Li_2Ir_{1-x}Rh_xO_3$ solid solution. *Solid State Sciences* **61**, 232–238 (2016).
19. Yogesh, S. *et al*. Relevance of the heisenberg-kitaev model for the honeycomb lattice iridates A_2IrO_3. *Phys. Rev. Lett.* **108**, 127203 (2012).
20. Singh, Y. & Gegenwart, P. Antiferromagnetic mott insulating state in single crystals of the honeycomb lattice material, Na_2IrO_3. *Phys. Rev. B.* **82**, 064412 (2010).
21. Takayama, T., Kato, A., Dinnebier, R., Nuss, J. & Takagi, H. Hyper-honeycomb iridate β-Li_2IrO_3 as a platform for kitaev magnetism. *Phys. Rev. Lett.* **114**, 077202 (2015).
22. Banerjee, A. *et al*. Neutron scattering in the proximate quantum spin liquid α-$RuCl_3$. *Science* **356**, 1055–1059 (2017).
23. Ramirez, A. P. Strongly geometrically frustrated magnets. *Ann. Rev, Mater. Sci.* **24**, 453–480 (1994).
24. Makintosh, A. R. & Andersen, O. K. *Electrons at the Fermi Surface*, vol. 149 (M. Springford, 1980).
25. Heiba, Z. K. & El-Sayed, K. Structural and anisotropic thermal expansion correlation of Li_2ZrO_3 at different temperatures. *Journal of Applied Crystallography* **35**, 634–636 (2002).
26. Jansen, V. & Hoppe, R. Z. Zur kenntnis der nacl-strukturfamilie: Neue untersuchungen an Li_2MnO_3. *Anorg. Allg. Chem.* **397**, 279 (1973).
27. Boulineau, A., Croguennec, L., Delmas, C. & Weill, F. Reinvestigation of Li_2MnO_3 structure: Electron diffraction and high resolution TEM. *Journal of Applied Crystallography* **21**, 4216–4222 (2009).
28. Hibble, S. J., Fawcett, I. D. & Hannon, A. C. Structure of two disordered molybdates, Li_2MoIVO_3 and $Li_4Mo_3IVO_8$, from total neutron scattering. *Acta Crystallographica* **B53**, 604–612 (1997).
29. O'Malley, M. J., Verweij, H. & Woodward, P. M. Structure and properties of ordered Li_2IrO_3 and Li_2PtO_3. *Journal of Solid State Chemistry* **181**, 1803–1809 (2008).
30. O'Malley, M. J. & Woodward, P. M. *A Structural, Bonding, and Properties Study of the Ordered Rock Salt Structures, Li2MO3 (M = Ru, Ir, Pt)* (Dissertation Thesis, Ohio State University, 2009).

31. Katukuri, V. M. *et al*. Strong magnetic frustration and anti-site disorder causing spin-glass behavior in honeycomb Li_2RhO_3. *Scientific Reports* **5**, 14718 (2018).
32. Lei, H., Yin, W.-G., Zhong, Z. & Hosono, H. Structural, magnetic, and electrical properties of $Li_2Ir_{1-x}Ru_xO_3$. *Physical Review B* **89**, 020409 (2014).
33. Larson, A. C. & Von-Dreele, R. B. General structure analysis system (GSAS). *Los Alamos National Laboratory Report* 86–748 (1994).
34. Toby, B. H. EXPGUI, a graphical user interface for GSAS. *Journal of Applied Crystallography* **34**, 210–213 (2001).
35. Treacy, M. M. J., Newsam, J. M. & Deem, M. W. A general recursion method for calculating diffracted intensities from crystals containing planar faults. *Proc. R. Soc. Lond. Ser. A* **433**, 499 (1991).
36. van der Laan, G. & Thole, B. T. Local probe for spin-orbit interaction. *Physical Review Letters* **60**, 1977 (1988).
37. van der Laan, G. & Thole, B. T. Orbital magnetism and spin-orbit effects in the electronic structure of $BaIrO_3$. *Physical Review Letters* **105**, 216407 (2010).
38. Laguna-Marco, M. A. *et al*. Orbital magnetism and spin-orbit effects in the electronic structure of $BaIrO_3$. *Physical Review Letters* **105**, 216407 (2010).
39. Gangopadhyay, S. & Pickett, W. E. Interplay between spin-orbit coupling and strong correlation effects: Comparison of the three osmate double perovskites Ba_2AOsO_6 (A = Na, Ca, Y). *Physical Review B* **93**, 155126 (2016).
40. Mazin, I. I., Jeschke, H. O., Foyevtsova, K., Valentí, R. & Khomskii, D. I. Na2IrO3 as a molecular orbital crystal. *Phys. Rev. Lett.* **109**, 197201 (2012).
41. Mazin, I. I. *et al*. Origin of the insulating state in honeycomb iridates and rhodates. *Phys. Rev. B.* **88**, 035115 (2013).
42. Yamaji, Y., Nomura, Y., Kurita, M., Arita, R. & Imada, M. First-principles study of the honeycomb-lattice iridates Na_2IrO_3 in the presence of strong spin orbit interaction and electronic correlations. *Phys. Rev. lett.* **113**, 107201 (2014).
43. Nishimoto, S. *et al*. Strongly frustrated triangular spin lattice emerging from triplet dimer formation in honeycomb Li_2IrO_3. *Nat. Commun.* **7**, 10273 (2016).
44. Hu, K., Wang, F. & Feng, J. First-principles study of the magnetic structure of Na2IrO3. *Phys. Rev. Lett.* **115**, 167204 (2015).
45. Kim, M., Kim, B. H. & Min, B. I. Insulating nature of Na_2IrO_3: Mott-type or slater-type. *Phys. Rev. B* **93**, 195135 (2016).
46. Li, Y., Winter, S. M., Jeschke, H. O. & Valenti, R. Electronic excitations in gamma-Li2IrO3. *Phys. Rev. B* **95**, 045129 (2017).
47. Gonze, X. *et al*. Abinit: first-principles approach to materials and nanosystem properties. *Comp. Phys. Commun.* **180**, 2582 (2009).
48. Gonze, X. *et al*. Recent developments in the ABINIT software package. *Computer Phys. Comm.* **205**, 106 (2016).
49. Perdew, J. P., Burke, K. & Ernzerhof, M. Generalized gradient approximation made simple. *Phys. Rev. Lett.* **77**, 3865 (1996).
50. Torrent, M., Jollet, F., Bottin, F., Zerah, G. & Gonze, X. Implementation of the projector augmented-wave method in the ABINIT code. *Comput. Mat. Science* **42**, 337 (2008).
51. Amadon, B., Jollet, F. & Torrent, M. Gamma and beta cerium: LDA + U calculations of ground-state parameters. *Phys. Rev. B.* **77**, 155104 (2008).
52. O'Regna, D. D. & Teobaldi, G. Optimization of constrained density functional theory. *Phys. Rev.* **94**, 035159 (2016).
53. Veiga, L. S. I. *et al*. Fragility of ferromagnetic double exchange interactions and pressure tuning of magnetism in 3d–5d double perovskite Sr_2FeOsO_6. *Physical Review B* **91**, 235135 (2015).

Acknowledgements

This work is supported by NSF DMREF Grant Nos DMR-1534711 (M.A.S), DMR-1534741 (A.P.R), DMR-1534719 (W.E.P.) and DMR-1534734(D.S.D). Work at Argonne is supported by the U.S. Department of Energy, Office of Science, Office of Basic Energy Sciences under Contract No. DE-AC-02-06CH11357. The authors would like to acknowledge ORNL for providing access to their neutron research facilities. For computation, the National Energy Research Scientific Computing Center (NERSC), a DOE Office of Science User Facility supported by DOE under Contract No. DE-AC02-05CH11231, as well as an in-house cluster at UC Davis, are gratefully acknowledged.

Author Contributions

M.A.S. and A.P.R. conceived the interest. M.K.W. designed, constructed, and carried out the synthesis. P.G.L. and M.K.W. collected electronic and magnetic properties. M.K.W. and J.L. performed TOF neutron refinements and M.K.W. performed stacking fault modeling. S.T.P. and W.E.P. performed DFT calculations. D.H. collected and analyzed XAS measurements. A.P.R., W.E.P., D.S.D., and P.G.L. analyzed and discussed electronic properties and M.A.S., M.K.W., and J.L. discussed structure characterization. All authors contributed to the manuscript.

Additional Information

Supplementary information accompanies this paper at https://doi.org/10.1038/s41598-018-25028-0.

Competing Interests: The authors declare no competing interests.

Publisher's note: Springer Nature remains neutral with regard to jurisdictional claims in published maps and institutional affiliations.